In situ CHARACTERISATION OF THREE-PHASE FLOW IN MIXED-WET POROUS MEDIA USING SYNCHROTRON IMAGING

A PREPRINT

May 3, 2020

Alessio Scanziani, Abdulla Alhosani, Qingyang Lin, Catherine Spurin, Gaetano Garfi, Martin J. Blunt and Branko Bijeljic.
Department of Earth Science and Engineering, Imperial College London, SW7 2AZ London.
alessio.scanziani16@imperial.ac.uk

ABSTRACT

We use fast synchrotron X-ray imaging to understand three-phase flow in mixed-wet porous media to design either enhanced permeability or capillary trapping. The dynamics of these phenomena are of key importance in subsurface hydrology, carbon dioxide storage, oil recovery, food and drug manufacturing, and chemical reactors. We study the dynamics of a water-gas-water injection sequence in a mixed-wet carbonate rock. During the initial waterflooding, water displaced oil from pores of all size, indicating a mixed-wet system with local contact angles both above and below 90°. When gas was injected, gas displaced oil preferentially with negligible displacement of water. This behaviour is explained in terms of the gas pressure needed for invasion. Overall, gas behaved as the most non-wetting phase with oil the most wetting phase; however pores of all size were occupied by oil, water and gas, as a signature of mixed-wet media. Thick oil wetting layers were observed, which increased oil connectivity and facilitated its flow during gas injection. A chase waterflooding resulted in additional oil flow, while gas was trapped by oil and water. Furthermore, we quantified the evolution of the surface areas and both Gaussian and the total curvature, from which capillary pressure could be estimated. These quantities are related to the Minkowski functionals which quantify the degree of connectivity and trapping. The combination of water and gas injection, under mixed-wet immiscible conditions leads to both favourable oil flow, but also to significant trapping of gas, which is advantageous for storage applications.

***K*eywords** Three-phase flow · Wettability · Porous media · Oil recovery · Gas storage · Minkowski functionals

1 Introduction

Three-phase flow in porous media is observed in many natural and engineered processes. These include non-aqueous phase liquid (NAPL) contaminant removal, gas storage in oil reservoirs, and enhanced oil recovery (EOR) [64]. EOR can be combined with gas storage, for example when storing CO_2 underground to mitigate climate change (carbon capture and storage, CCS) [71]. In this case, it would be ideal if high oil recovery is combined with significant gas storage [65, 10]. Since depleted hydrocarbon fields contain injection infrastructure, CCS is an attractive option with the potential economic benefit of additional oil recovery: combining CCS with EOR could be a key technology to enable storage at the gigatonne scale necessary to make a significant impact on preventing dangerous climate change [21, 67, 19].

The flow of three fluid phases - two liquids and a gas - is also important in many manufacturing contexts, to synthesize emulsions containing droplets and micro-bubbles, for food manufacture [79], drug delivery [31] and the synthesis of micro-capsules [28]. Microfluidics devices can be designed to form porous media of desired structure and composition, controlled by the interaction of wettability, flow and pore space topology. Three-phase flow is also encountered in

packed bed reactors and catalysis with applications in biological waste water treatment and fluid separation, for instance [41].

The optimisation of these processes can be achieved only with an accurate study of the flow and trapping of the three phases, bearing in mind that the physics controlling the flow are defined at the micron scale of the pore space [22]. Previous studies have used micromodels to investigate three-phase flow in porous media, at the pore scale. Øren *et al.* [54] visualized the formation of spreading oil layers, in a quasi two-dimensional water-wet micromodel. The formation of spreading layers around droplets has also been observed in microfluidics devices [28]. Other studies have identified the occurence of multiple displacements (when one phase displaces another which in turn displaces the third one) in micromodels with variable wettability [70, 74].

However, the use of micromodels may not capture the intricate behaviour of multiphase flow in the complex pore space of three-dimensional porous media which include rocks, soils and catalysts. Advances in both X-ray imaging and associated analysis methods which allow direct *in situ* visualization of the pore space, and the fluids within it, have revolutionized our understanding of flow in porous media [26, 78, 55]. Previous work on two-phase (oil and water, or CO_2 and water) flow with application to improved carbon dioxide storage and oil recovery highlighted the crucial role of wettability as a determinant of flow behaviour, trapping and recovery [57, 7, 3]. In particular, mixed-wettability – where the solid surface has regions that are both water-wet and oil-wet, indicating contact angles between oil and water both above and below 90° – leads to well-connected oil and water phases and favourable oil recovery [52, 40, 62]. The fluid-fluid interfaces have almost zero mean curvature, with approximately equal but opposite principal curvatures in orthogonal directions, forming minimal surfaces [46].

However, further complexities arise in three-phase flow, where the interaction among three phases at their interface strongly influences multiphase flow phenomena, and eventually oil flow and gas trapping. The spreading coefficient of a phase i, C_{si}, defines if the phase i is allowed to form spreading layers sandwiched between the other two [36, 29]. The formation of these layers is favoured if $C_{si} \approx 0$ [1]. In this study we will employ fast synchrotron tomography to examine the dynamics of layer formation in mixed-wet media.

One principal characteristic of three-phase flow, which will be emphasis of this paper, is the wettability order according to which different phases arrange in pore space [72, 56]. The wettabilty of a phase with respect to another is directly defined by the contact angle θ at their interface [22, 11, 63]. The wettability order defines which phase more favourably wets the surface of the rock and which one instead preferentially resides in the centre of the pores [72]. This arrangement of the phases in the pore space has consequences on their flow, and hence the relative permeability of each phase [30, 37, 6]. Pore occupancy, defined as a relation between the dimension of the pores and the phase which occupies them, can be provided by X-ray tomography and used to identify the wettability order in three-phase flow [27, 64, 4]. The phase which occupies the smallest pores is the most wetting phase, while the least wetting phase preferentially occupies the largest pores. The most non-wetting phase has the largest flow potential while it is connected, but can also be trapped by the other phases, adding to storage security, for instance.

In three-phase flow, *in situ* pore-scale imaging studies have been concerned, to date, principally with water-wet media [24, 6]. In this case the wettability order is water-oil-gas from most to least wetting [39, 64, 4]. In water-wet media, as previously observed in micromodels [54, 29] and porous rocks [64], oil can form spreading layers sandwiched between water that wets the surface and gas that preferentially fills the larger pores. Gas can become trapped by both oil and water. Indeed, since spreading oil layers can completely wet the gas, the trapping of gas can be enhanced compared to two-phase gas-water displacement, which provides a rapid and secure mechanism to retain gas in the subsurface for storage [65, 9]. Even if the majority of oil fields are not water-wet, only a few studies have investigated the effect of wettability alteration on three-phase flow. Qin *et al.* [57] studied gas and water injection in a weakly oil-wet carbonate. They observed favourable oil recovery by gas injection as a result of gas-oil-water double displacement processes, with further recovery combined with gas trapping after subsequent waterflooding. They studied the static arrangement of the phases at the end of each injection. However, the evolution of the pore-scale arrangement of the phases during a displacement was not studied.

The use of bright X-rays at synchrotron sources allows for images to be taken with a time resolution of approximately 1 minute and hence it is a powerful technique to study the dynamics of multiphase flow [77, 20, 14]. In particular, it has capability to visualize and quantify how displacement proceeds on a pore-by-pore basis providing great insight into two-phase flow processes [69, 60, 12]. We will extend the use of synchrotron imaging to the simultaneous flow of three phases in mixed-wet media.

Advances in visualization have been complemented by analysis methods derived from algebraic topology [16]. Specifically, the measurement of Minkowski functionals links the geometry and topology of pore space with physical quantities, such as the connectivity of the fluid phases [51, 51, 49]. Considering a solid in Euclidean three-dimensional space, four Minkowski functionals are defined: volume, surface area, total curvature and Gaussian curvature [75]. We will

Table 1: Physical properties of the fluids used in the experiments. Densities measured at 40° and 7.6 MPa. Viscosities of nitrogen and water at 50° and 10 MPa from [34] and of decane at ambient condition from [53]. The interfacial tensions were measured directly using the pendant drop method [45, 4].

Phase	Density $[kg/m^3]$	Viscosity $[mPa \times s]$	Interfacial tension $[mN/m]$
Water (H_2O + 20%w KI)	1154.05	0.5471	$\sigma_{ow} = 52.1$
Oil (Decane + 15%w $C_{10}H_{21}I$)	715.2	1.088	$\sigma_{go} = 11.2$
Gas (N_2)	83.98	0.01896	$\sigma_{gw} = 63.7$

use this set of measures to provide a complete characterisation of the phases within the pore space, realating the topological information with physical characteristics of the flow and trapping such as saturations, capillary pressure and connectivity.

The main objective of this study is to understand the dynamics of three-phase flow in mixed-wet porous media and how this is controlled by the wettability order. To this end, we employ fast synchrotron tomography to study gas injection followed by water injection in a mixed-wet carbonate sample. Scanziani *et al.* [65] performed synchrotron experiments of three-phase flow on a similar carbonate rock under water-wet conditions, observing the dynamics of the formation of spreading oil layers and the double capillary trapping of gas. We seek to understand the key determinants governing displacement, namely the effect of wettability on pore occupancy and formation or break up of fluid layers. Furthermore, we discuss how these pore-scale phenomena exert an impact on flow and trapping. We will compare and discuss our results in light of previous measurements made on a similar water-wet system [64, 65] and the same rock under near-miscible conditions [4], using the Minkowski functionals to quantify our observations. Finally, we will place our work in context by exploring the implications for storage, recovery, and the performance optimization of manufactured porous devices.

2 Materials and methods

We used a cylindrical sample of Ketton limestone, with a length of 22 mm and a diameter of 5.8 mm. The total porosity was measured to be 28.3% with a Helium porosimeter, while the apparent porosity obtained with image processing was 14.3%. This latter value represents the porosity of the macro-pores resolvable in the image; the oolithic grains of the rock are also porous, but these micro-pores cannot be explicitly seen in the images. We assume that the microporosity is water-saturated throughout the experiment. The sample was initialized with the injection of formation brine, prepared to mimic the chemical composition of the brine in a giant producing oil reservoir in the Middle East.

2.1 Establishing wettability

A process called ageing was performed to restore the wettability conditions typically encountered in hydrocarbon reservoirs [47, 2]. This was achieved using crude oil provided from the same producing reservoir from which the brine composition was taken. More information on crude oil composition are provided by Alhammadi *et al.* [2]. Pressure and temperature were raised to the conditions representative of an oil field deep underground (10 MPa and 80 $^\circ C$). Crude oil was then injected through the sample, increasing the flow rate step-wise from 0.01 to 0.1 mL/min at the bottom of the sample. The flow was then reversed and more crude oil was injected at the top of the sample, at the same flow rates. For a week, 5 pore volumes, PV, of crude oil were injected each day. The sample was then left at these conditions of high temperature and pressure for a month and then conserved in an oven in the crude oil at ambient pressure and 80 $^\circ C$ for 2 months.

2.2 Experimental fluids

After ageing, the sample was transferred to the Diamond Light Source synchrotron facility in the UK, where the experiments were performed. The experimental fluids used were pure nitrogen, water doped with 20% by weight potassium iodide (KI), and decane doped with 15% by weight iododecane ($C_{10}H_{21}I$). These dopants provided sufficient difference in the X-ray attenuation of each phase, so that they could be distinguished in the final images [64]. The properties of the fluids used are listed in Table 1: the interfacial tensions were measured using the pendant drop method [45, 4].

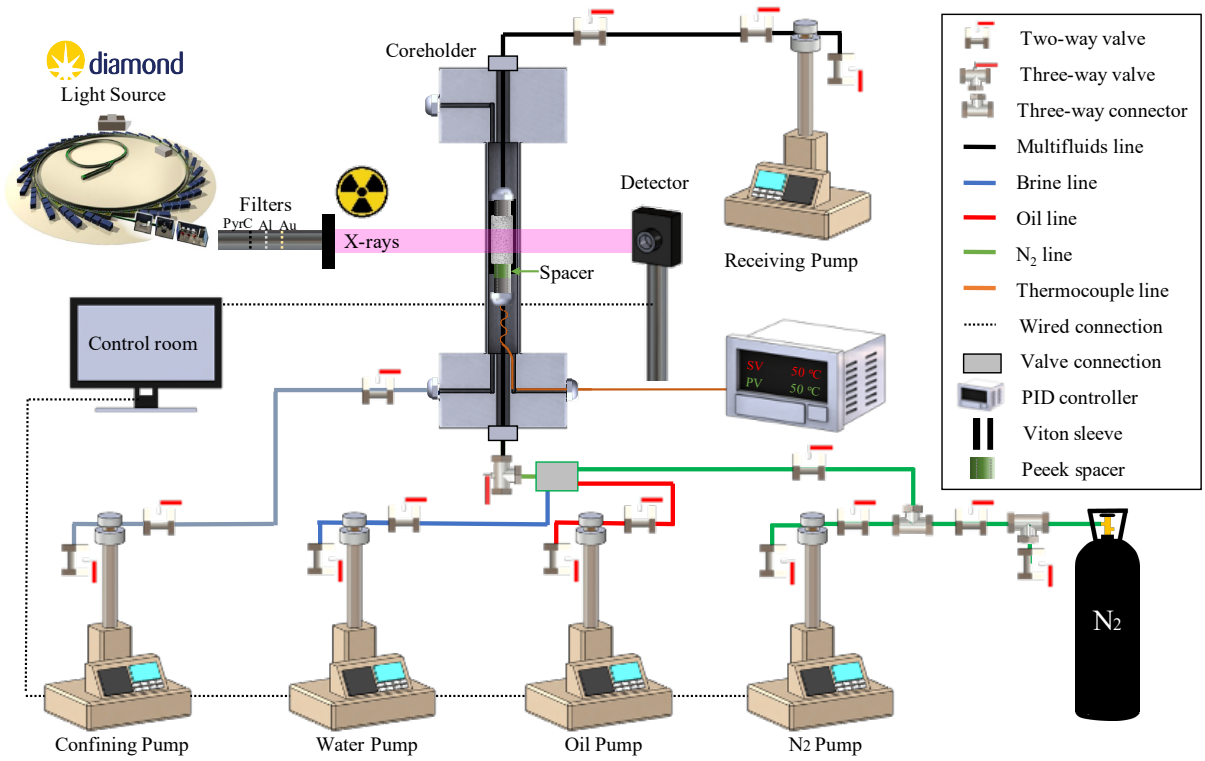

Figure 1: Schematic of the experimental apparatus comprising three injection pumps, a receiving pump and a confining pump to maintain high fluid pressures. The sample is imaged using synchrotron X-rays.

2.3 Experimental method

Figure 1 illustrates the experimental apparatus. The three-phase flow experiments were performed while imaging the sample using high energy X-rays. The sample was mounted inside the coreholder (Figure 1) on top of a PEEK spacer, which was used during imaging to identify the exact times at which the fluids invaded the sample. Before starting the synchrotron tomography experiment, the oil was injected in the sample to displace and substitute the crude oil.

Pressure and temperature were then raised to the experimental conditions, 8 MPa and 50°C, and water injection (WF1) was started at 0.5 $\mu L/min$, corresponding to a capillary number $Ca = 3.3{\times}10^{-9}$ defined by $Ca = \mu q/\sigma$ where q is the Darcy flow rate, μ is the viscosity of the injected phase (doped brine, the water phase), and σ is the oil-water interfacial tension (see Table 2). All the injections were performed from the bottom of the sample. When water was detected in the PEEK spacer, dynamic imaging of the centre of the sample (Figure 2) started. WF1 was stopped after 78 minutes (0.5 pore volumes, PV, injected), when no significant change in the pore space had been observed for at least 15 minutes. This was assessed by checking differential images between scans taken 10 minutes apart from each other. Gas injection (GI) was then performed at a flow rate of 0.15 $\mu L/min$ ($Ca = 1.6{\times}10^{-10}$ using the gas flow rate and viscosity, and the gas-oil interfacial tension), for 92 minutes (0.2 PV). Second waterflooding (WF2) was then performed at 0.1 $\mu L/min$ ($Ca = 2.0 \times 10^{-9}$ using the water flow rate and viscosity, and the water-oil interfacial tension) for 204 minutes (0.3 PV).

2.4 Synchrotron imaging

The imaging was performed at the Diamond Manchester Imaging Branchline (I13-2). High intensity X-rays were collected from the accelerator machine of the Diamond Light Source and brought to the beamline. Here, three filters (1.3 mm Pyrolytic C, 3.2 mm Al and 10 μm Au) trimmed the wavelength of the X-rays to obtain a high intensity pink beam [50]. The resulting X-ray spectrum has a thin peak at 15 keV, corresponding to a flux of 9×10^{12} photons per second [59]. The distance between the sample and the camera was set to provide optimal image quality.

High quality static images were collected before and after each injection step, scanning the whole sample with three scans at the predetermined locations in the vertical direction, and these were later stitched together to obtain images of

Table 2: Experimental and imaging details. The capillary number is defined by $Ca = \mu q/\sigma$ where q is the Darcy flow rate of the injected phase and μ is the viscosity of the injected phase. We used the oil-water interfacial tension σ_{ow} to calculate Ca during WF1 and WF2 and the gas-oil interfacial tension, σ_{go} to calculate Ca during GI (see the values in Table 1). PV is the number of pore volumes injected. The saturations, S_w, S_o and S_g are computed from the segmented images at the end of each injection.

Displacement	Flow rate $[\mu L/min]$	Ca	PV	S_w	S_o	S_g
WF1	0.50	3.3×10^{-9}	0.5	0.34 ± 0.02	0.66 ± 0.03	-
GI	0.15	1.6×10^{-10}	0.2	0.33 ± 0.02	0.43 ± 0.03	0.24 ± 0.03
WF2	0.30	2.0×10^{-9}	0.3	0.38 ± 0.02	0.39 ± 0.03	0.23 ± 0.03

Table 3: Details on the time of each of the three dynamic imaging steps. Three static scans were collected at the end of each step. The exposure time is the time taken to image one projection: a three-dimensional image is then constructed from all the projections. Values for number of projections and exposure time are reported for both S = static images and D = dynamic images.

Displacement	Time begin, time end $[s]$	Images	Projections (S-D)	Exposure time (S-D) $[s]$
WF1	0, 4706	65	3000 - 900	0.08 - 0.06
GI	5627, 9553	56	2000 - 900	0.08 - 0.06
WF2	10665, 18074	106	3000 - 1000	0.08 - 0.06

the whole sample (Figure 2). Each static image contains $1284 \times 1286 \times 2044$ voxels. During the injections, dynamic imaging was performed at the middle of the sample in the vertical direction, as illustrated in Figure 2. The spatial resolution of all the images was 3.5 μm, while each dynamic scan was taken every 74 s (WF1 and GI) or 80 s (WF2): the time required to acquire each scan is obtained by multiplying the exposure time per the number of projections, provided in Table 3, with 20 s required to bring the sample back to the initial position and transfer the data from the detector to the workstation in the control room. Each of these dynamic images contains $1200 \times 1240 \times 1080$ voxels.

We collected a total of 227 tomograms over the whole experiment. The time stamp of each injection sequence and the number of tomograms are listed in Table 3.

2.5 Image processing

All the tomograms were reconstructed, obtaining three-dimensional grey scale images. Segmentation - the assignment of each voxel to a phase (rock, water, oil or gas) - was then required to obtain the quantitative results presented in Section 3.

The static scans were segmented using a seeded watershed segmentation algorithm [38]. Prior to segmentation, these images were stitched together to obtain the full image of the sample and filtered with a non-local means filter [25, 66]. Injected water and gas were identified by subtracting the image obtained at the beginning of the experiment from images acquired at the end of WF1, GI and WF2. The result was filtered again with the non-local means filter prior to performing watershed segmentation [25].

The quality of the images obtained during the injection of fluids was lower, as we minimised the acquisition time to capture the dynamics. For this reason, another, more accurate but time consuming, segmentation method was required for these images: we used the machine learning WEKA segmentation method [13]. The preliminary steps were similar, as we performed subtraction of the image at initial condition to each of the dynamic images. However, filtering was not required, as WEKA segmentation method has a filtering step embedded. A sample image was manually labelled, to construct the training data set. A random forest machine learning method was then applied to the image that uses the training data set to classify all the voxels in the images. The two segmentation methods give comparable results when applied to the same images [2, 32].

The segmented images were post-processed to obtain quantitative results. The saturation of each phase was obtained from the images by computing the fraction of voxels assigned to the selected phase in relation to the total number of voxels assigned to the pore space. The water volume in micro-porosity was ignored in the analysis. Connectivity was obtained by selecting one phase and assigning its voxels to connected clusters (or ganglia).

To obtain information on the dimension of pore openings (pores) or restrictions (throats) occupied by each phase, the pore space was mapped using a generalised pore-network model [58], obtaining sets of maximum balls representing

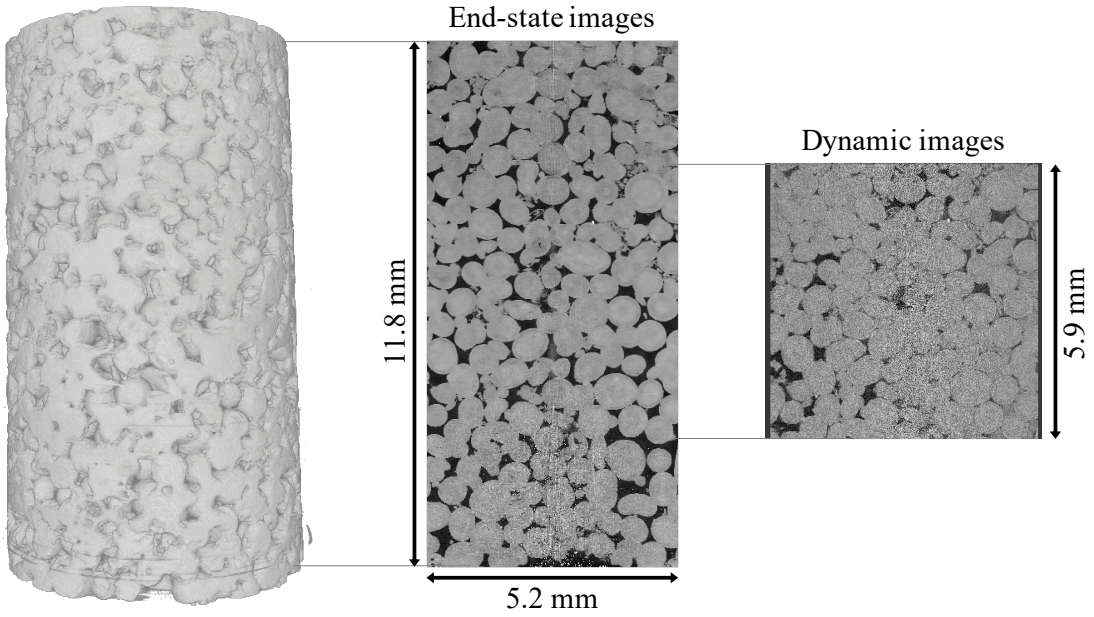

Figure 2: Static images were collected at the end of each injection, at three different locations in the vertical direction, and stitched together to obtain images of the whole sample. These images were used to compute saturation, Table 2. Dynamic images were acquired during the injections in a selected location at the centre in the vertical direction.

pores and throats, with their inscribed diameter. This *equivalent pore diameter* will be used as a proxy for pore dimension. Combining this map with the three-dimensional images of the pore space, pore and throat occupancy were obtained from identifying the phase that occupied the voxel at the centre of the maximal ball [64]. A similar maximum-ball concept was used to identify the local thickness of the oil phase and obtain the oil layer thickness: the maximum ball that can be inscribed in the space identified with oil in each location is the local oil thickness [35].

The interface between the phases was identified as the surfaces meshed on voxels which have neighbours assigned to different phases (interfacial voxels). The interface was smoothed to remove voxelization artefacts [48]. The specific interfacial area was computed as the total area of the surface of the interface between two phases divided by the total volume of the rock (pore and grain).

We define the total curvature between phases i and j as κ_{ij} with a positive value when phase j bulges into phase i, and use it to estimate the capillary pressure $P_{c,ij} = P_j - P_i = \sigma_{ij}\kappa_{ij}$ from the Young-Laplace eqaution [43] where σ_{ij} is the interfacial tension between phases i and j. There is a general constraint between the curvatures if the phases are connected:

$$\sigma_{ik}\kappa_{ik} = \sigma_{ij}\kappa_{ij} + \sigma_{jk}\kappa_{jk}. \tag{1}$$

The total curvature is defined as the sum of the two curvatures in the two principal directions, while the Gaussian curvature is the product of the two principal curvatures [48, 17]. When computing both Gaussian and total curvatures, we record the interfacial area-weighted average values.

3 Results and discussion

We will now examine the pore-scale physics leading to either the enhancement of flow or trapping in mixed-wet porous media. The 227 tomograms obtained during the experiment were segmented as described in Section 2.5 and used for computing pore-scale descriptors and to interpret the dynamics of three-phase flow and trapping in mixed-wet porous media. After a first waterflooding (WF1), gas was injected in the sample to study three-phase flow (GI), followed by further injection of water (WF2). The three-dimensional (3D) configuration of the phases at the end of each injection is illustrated in Figure 3.

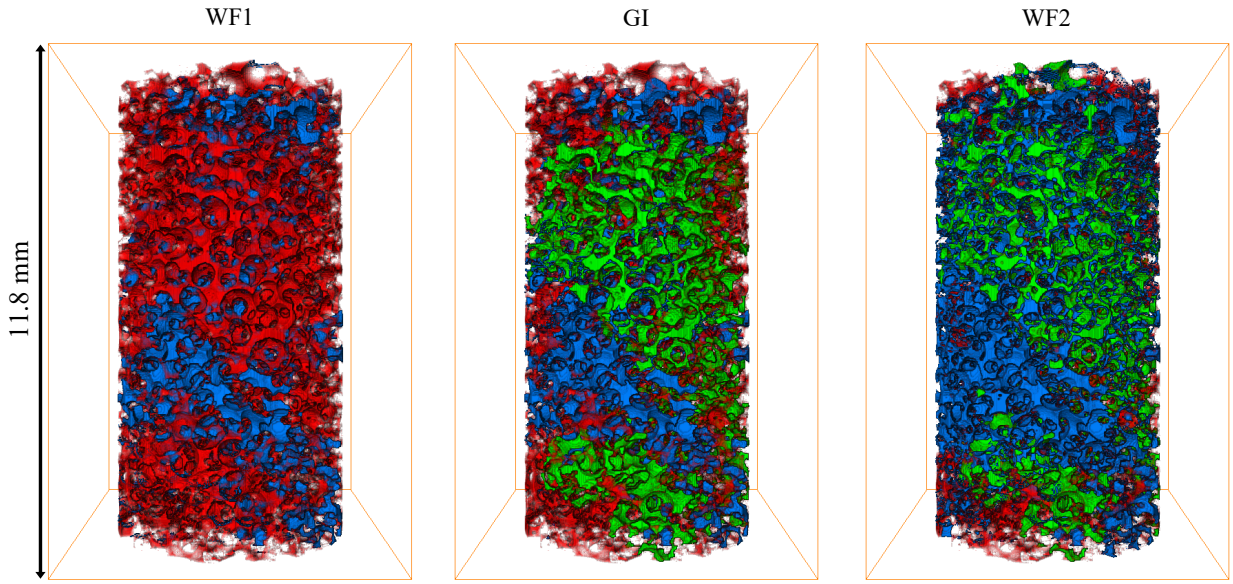

Figure 3: Three-dimensional rendering of oil (red), water (blue) and gas (green) at the end of first waterflooding (WF1), gas injection (GI) and second waterflooding (WF2).

First, in Section 3.1 we characterize the wettability of the sample. In Section 3.2 we study the dynamics of gas and water invasion during GI and WF2. Section 3.3 focuses on the formation and the thickness of oil layers, which allowed for oil recovery and Section 3.4 shows how gas is trapped in the pore space during WF2, ensuring a high remaining gas saturation, see Table 2. In Section 3.5, we use the four Minkowski functionals of a 3D object – volume, surface area, total curvature and Gaussian curvature – to obtain a complete characterisation of the dynamics of three-phase flow. The overall context of the work is how the wettability order controls the pore-scale fluid dynamics and the implication this has, in turn, for storage, recovery and design applications.

3.1 Wettability characterisation

The wettability of the system has a strong influence on the flow of the phases, their relative permeability and their trapping [37, 72, 56, 6]. The direct measure of wettability, defined for two-phase flow, is the contact angle between the interface of the two phases and the solid [11, 63, 7, 61]. The geometric oil-water contact angle for this sample was measured using the method of AlRatrout *et al.* [8] and resulted in a distribution of angles both lower and higher than 90° with a mean value of 109°, at the end of WF1. This defines the system as mixed-wet, as both oil and water can in turn favourably wet the solid surface at different locations in the sample. Figure 4 shows the probability distributions of the geometric contact angles between the phases at the end of GI and WF2, while Table 4 reports their mean values. These values suggest that, on average, water is the non-wetting phase with respect to oil, oil is wetting to gas, while water and gas present an intermediate wettability between each other, with mean values of contact angle close to 90°.

The contact angles in a three-phase system, θ, are not independent, but must obey the Bartell-Osterhof constraint in equilibrium [18, 73]:

$$\sigma_{ik}\cos\theta_{ik} = \sigma_{ij}\cos\theta_{ij} + \sigma_{jk}\cos\theta_{jk}, \tag{2}$$

for any phases i, j and k.

We use the interfacial tension values in Table 1 and the mean contact angles presented in Table 4 to predict the gas-water contact angle from the measured oil-water and gas-oil values [72]. There is a difference of about 15° degrees between the observed and predicted values: the direct measurements imply that on average gas is non-wetting to water (albeit weakly so), while the predictions of Eq. (2) suggest that gas is slightly wetting to water. However, the Bartell-Osterhof Eq. (2) is defined for three phases in equilibrum at the same location in a system with constant wettability. This is not the case for the mixed-wet medium studied here, where it has been shown that contact angles are variable in space and wettability is not constant through the whole sample.

Furthermore, the contact angles are measured at static conditions and so may represent hinging angles on rough or altered-wettability surfaces, rather than contact angles for a displacement process [23]. In particular, it is possible that

Table 4: Mean values and standard deviations of the contact angles measured in degrees at the end of each injection step for oil-water (θ_{ow}), gas-oil (θ_{go}) and gas-water (θ_{gw}) solid contacts, using the method developed by AlRatrout *et al.* [8].

Displacement	θ_{ow} [°]	θ_{go} [°]	θ_{gw} [°]	Predicted θ_{gw}, using Eq. 2 [°]
WF1	109 ± 23.2	-	-	-
GI	105 ± 27.5	57.1 ± 25.7	80.7 ± 23.2	96.9
WF2	103 ± 27.4	57.1 ± 24.1	81.9 ± 22.3	95.3

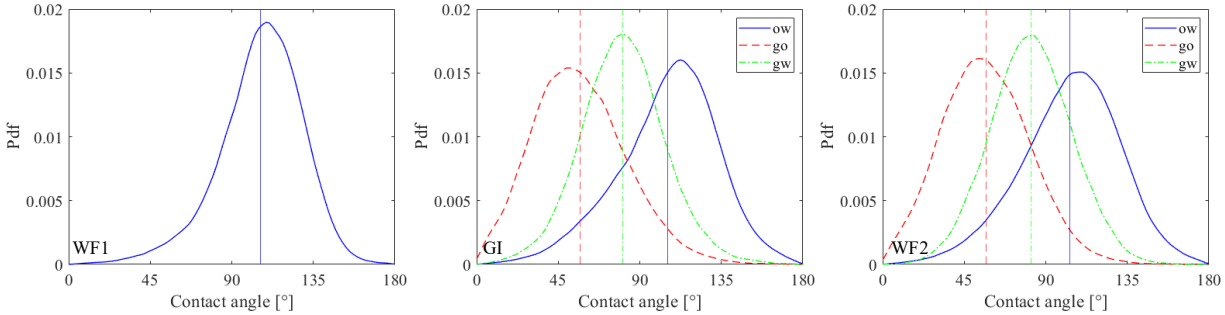

Figure 4: Geometric contact angles computed from the static images at the end of each injection, WF1, GI and WF2, for oil-water (ow), gas-oil (go) and gas-water (gw) solid contacts. The vertical lines represent the mean values.

high hinging oil-water contact angles are measured at the end of WF1, when the water pressure is high. These values, which do not represent the angles during a displacement, particularly at the early stages [62] persist in later injection sequences, which leads to an over-prediction of the actual gas-water contact angles using Eq. (2). However, this still represents some ambiguity in the wettability order: is gas more or less wetting than water?

In three-phase flow, the wettability order establishes which of the three phases more favourably flows on the surface of the rock grains, and in which order the other phases tend to reside in the centre of the pores and where they can be trapped. Using the directly-measured values of contact angles described previously, we notice that oil is wetting to both water and gas, water is non-wetting to oil and neutrally wetting to gas, while gas is non-wetting to oil and neutrally wetting to water. We would then expect that oil is the most wetting phase and gas and water are both, on average, non-wetting.

To further clarify the wettability order of the system, we used pore occupancy (Figure 5), fluid-solid interfacial areas (Figure 6a) and visual inspection (Figure 6b-c).

Pore occupancy has been previously used in three-phase flow to describe the arrangement of the three phases in the pore space [64, 4]. Figure 5 shows the pore occupancy at the end of each injection. We observe that we do not have a clear definition of most- and least-wetting phases. Water occupied pores of a wide range of sizes, while oil and gas preferentially resided in smaller and wider pores respectively. Using the mean value of the diameter of the pores occupied by each phase at the end of WF2, when all the phases have a similar saturation (Table 2), we can establish an approximate wettability order: oil- water- and gas-occupied pores had an average diameter of 35.7 ± 24.9, 49.4 ± 33.6 and 79.1 ± 24.5 μm respectively. Using these values we can suppose an oil-water-gas wettability order, from most- to least-wetting, but the high standard deviations suggest that there is a mix of wettabilities, as evident in WF1, with regions of the pore space that are wetting to oil, and regions that are water-wet.

The pore occupancy quantification method described above searches for the phase residing in the centre of the pores. With a different approach, we can study which phase preferentially wets the surface of the grains [33]. Figure 6a shows the interfacial area, specific to volume, between each of the three phases and the solid surface, computed from the segmented images, throughout the injection sequence. Oil was the phase with highest interfacial area with the solid at all times, confirming that it is, on average, the most wetting phase. This area decreased as gas was injected in the sample, but was still twice the area between water or gas and the solid, even when the oil saturation approached the water saturation at the end of GI, Table 2. The gas-solid interfacial area increased as gas was injected, approaching the water-solid value. Since the gas saturation at the end of GI was still lower than the water saturation (0.23 versus 0.37) we cannot definitely state that gas was less wetting than water, as its lower interfacial area with the solid would suggest. However, this approach again suggests an average oil-water-gas as the wettability order, consistent with the measured contact angles and assessment of pore occupancy.

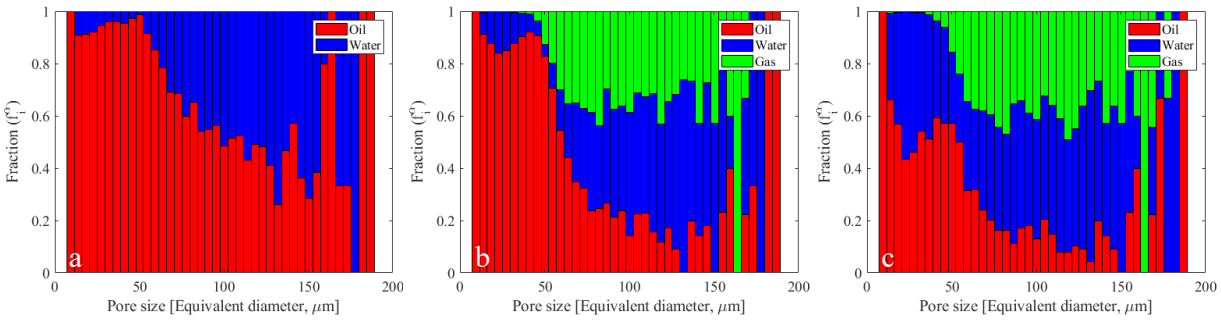

Figure 5: Pore occupancy at the end of (A) WF1, (B) GI and (C) WF2.

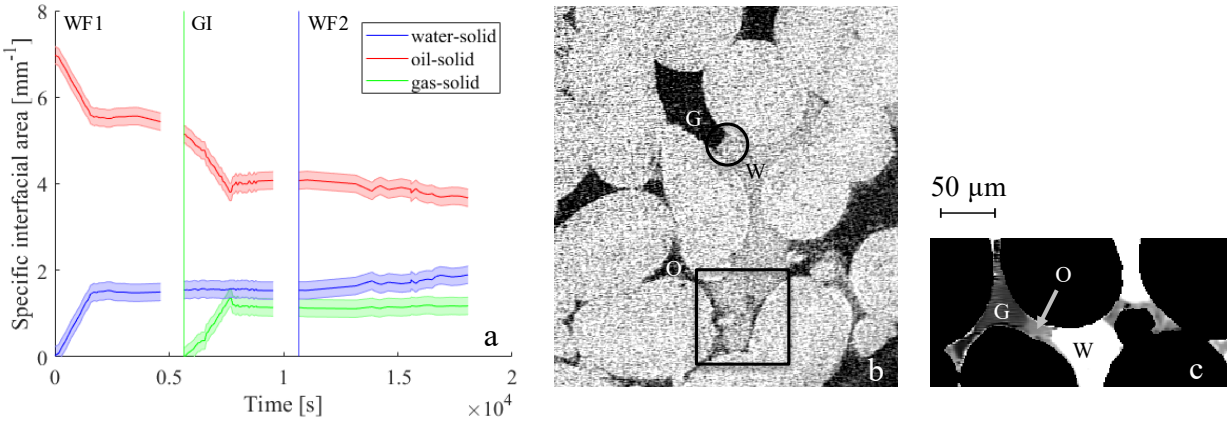

Figure 6: A: the interfacial area between each phase and the solid, normalised to the total image volume; the width of the lines indicate the uncertainty in the measurements. B: Two-dimensional slice of the grey scale image at the end of WF2, where G=gas, W=water and O=oil. C: Another slice of the grey scale image at the end of WF2, where the rock phase has been masked out for easier visual inspection. G=gas, W=water and O=oil.

Another indication of the wettability order can be inferred from direct visual inspection of the images of the rock and the fluids (Figure 6b-c). In the circled example of Figure 6b, as we noticed in many other locations in the pore space, an approximately flat interface between gas and water is shown, with a contact angle close to 90°. This suggests neutral wettability between these two fluids, which is consistent with the gas-water contact angle, the occupancy of pores of similar size (Figure 5) and similar fluid-solid interfacial area (Figure 6a), described earlier. In the squared detail of Figure 6b, we observe the presence of oil layers, wetting the solid surface. This is again consistent with the occupancy of pores of similar size and large oil-surface interfacial area, supporting the argument of oil being the most wetting phase. The formation and thickness of layers will be discussed in Section 3.3. In Figure 6c, gas-oil and water-oil interfaces are shown, where oil is wetting to both water and gas.

All the different methods of wettability characterisation illustrated above (contact angles, pore occupacy, fluid-solid interfacial area and visual inspection) consistently suggest an average oil-water-gas wettability order. However, the geometrical and chemical complexity of the pore space of rocks with altered wettability allows for a spatial variability of wettability through the sample, resulting in wide distributions and high standard deviations for contact angles, pore occupancy and interfacial areas. This variability defines the system as mixed-wet, and allows for complex behaviour of multiphase flow, with regions of the pore space that are, locally, more water-wet and, at the other extreme, regions where water is non-wetting to gas.

3.2 Dynamics of three-phase flow

Having defined the system as mixed-wet, with an average wettability order oil-water-gas, in the next sections we will describe the dynamics of three-phase flow during the injection steps and how some key pore-scale descriptors – related to the Minkowski functionals – dynamically changed during the injections. A complete description of the dynamics of

WF1 is provided by Scanziani *et al.* [62], while here we will focus on gas injection and second waterflooding, where three-phase flow is present.

3.2.1 Gas injection

The principal displacement process during gas injection was direct piston-like displacement of oil by gas (top row of Figure 7). This contrasts with the observations made in a weakly oil-wet sample [57] and in a previous study using the same Ketton rock under water-wet conditions [65] where double displacement events were common, in particular double drainage where gas displaced oil that displaced water [54]. The reason for this is the wettability of the system. After contact with crude oil, much of the pore space becomes oil-wetting, see Figure 4. This means that at the end of waterflooding, the capillary pressure $P_{cow} = P_o - P_w$ is negative – the water pressure is *higher* than the oil pressure, as water has to be forced into the pore space. When gas is now injected, gas will fill pores for whom the entry pressure allows invasion at the lowest gas pressure. If P_{cow} remains unchanged, then it is more favourable for gas to displace oil, as it has a lower pressure than water, especially as gas is non-wetting to water in most of the pore space and has to have a higher pressure than water to displace it. Double displacement is suppressed thanks to contact angle hysteresis: the contact angle for oil to re-invade water occupied pores is likely to be lower – meaning less favourable displacement – than during waterflooding [52]. This interpretation of the results will be confirmed later when we quantify capillary pressures.

The bottom row of Figure 7 shows the occupancy of the throats or restrictions in the pore space during GI: this contrasts with Fig. 5 which showed the occupancy of the wider regions, pores. At the end of WF1 water had invaded a wide range of throat size [65], as a signature of mixed wettability. The injected gas, being the most non-wetting phase, would be expected to invade the largest throats preferentially. However, even if most of the largest throats were indeed invaded by gas at the end of GI, gas also invaded some smaller throats; this is most noticeable at the beginning of GI. The reason for this behaviour is twofold: first, not all the throats are available for displacement at any time, as some throats are either far from the gas front or occupied by water (hence requiring higher capillary pressure). Secondly, the wettability of the sample is not constant in space, but this is instead characterised by a wide spatial distribution of contact angles (Figure 4). This means that some smaller throats which are less non-wetting to gas will fill preferentially to larger throats where the gas-oil contact angle is closer to zero.

3.2.2 Second waterflooding

Again, unlike the water-wet case, the principal displacement process during WF2 is direct displacement of oil by water; there is little contact between water and gas, as the gas is surrounded by wetting and spreading layers of oil - described in the next section. We observed some double displacement events – water-gas-oil – as seen in water-wet rocks as well [64, 65], where water displaces oil that traps gas. This causes oil layers to swell and trap gas by snap-off. A detailed description of this trapping mechanism will be provided in Section 3.4.

3.3 Layers

In this section we will study oil layers since they can enhance oil connectivity and flow, while facilitating the trapping of water and gas. From Table 1 can define a spreading coefficient C_{si} for phase i in the presence of phases j and k as follows [22, 36]:

$$C_{si} = \sigma_{jk} - \sigma_{ij} - \sigma_{ik}. \tag{3}$$

Using the values in Table 1 we calculate an oil spreading coefficient $C_{so} = 0.2$ mN/m. This is close to zero and indicates that it is possible for oil to spread between water and gas in the pore space. Furthermore, under oil-wet conditions, the oil can reside next to the solid surface with gas or water occupying the centre of the pore space.

At near-miscible conditions, when the properties of the gas and oil are similar, it is possible to observe layers of gas [5]. However, in our experiments, where oil and gas are immiscible, using Eq. 3 and Table 1, $C_{sg} = -22.7\ mN/m$ which is large and negative, indicating that gas layers will not form. The spreading coefficient for water, the intermediate wetting phase, is even more large and negative ($C_{sg} = -104.7\ mN/m$), making it very unfavourable for water layers to exist.

The arrangement of a phase in layers causes an increase in its connectivity, allowing the flow in the pore space at low relative permeabilities. For three-phase flow in a water-wet medium, with a wettability order water-oil-gas from most wetting to most non-wetting, spreading oil layers have been observed [64]. However, with the same wettability order, under near-miscible conditions, oil layers were not observed during gas injection, with oil and water confined to the smaller pores [4].

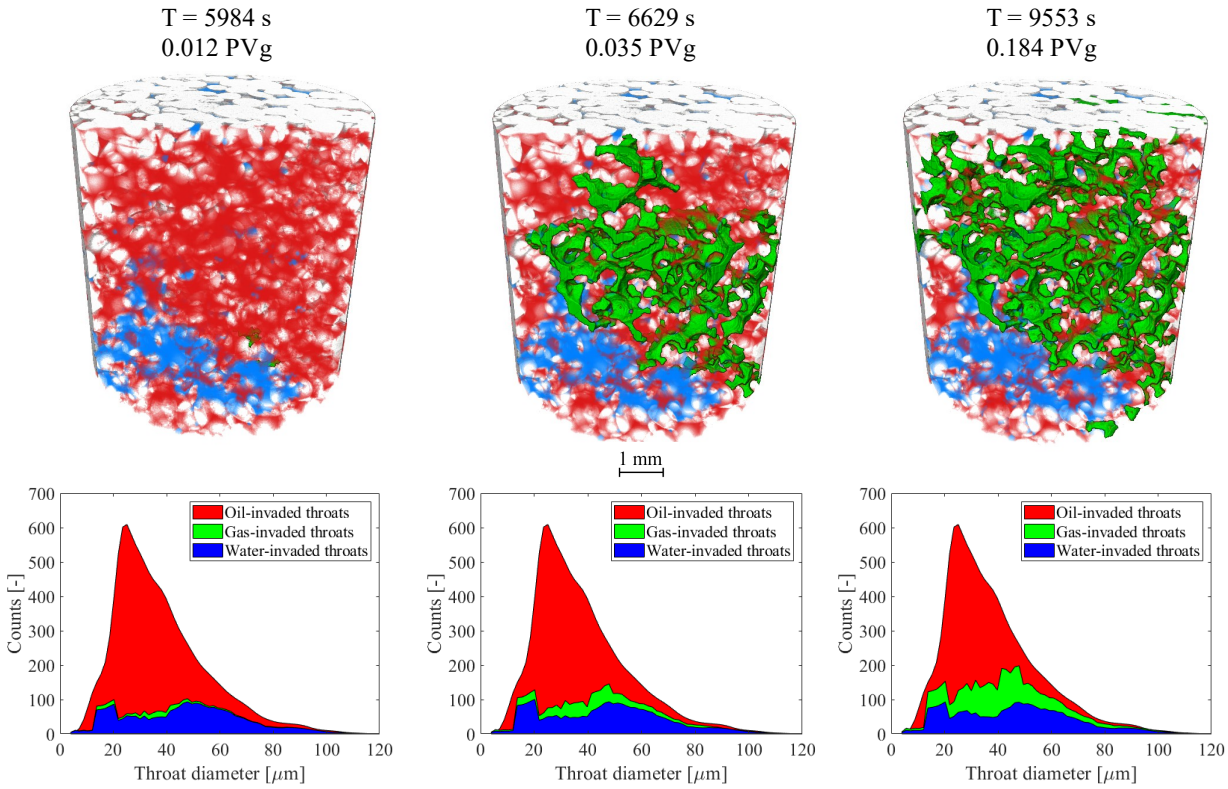

Figure 7: Top row: three-dimensional rendering of the rock (light grey), oil (red), water (blue) and gas (green) at different times during GI. Bottom row: area chart showing the distribution of throat size and their occupancy. PVg indicates the pore volumes of gas injected at each time step.

In this system we did not observe any layers of gas, as the gas was not everywhere the intermediate wetting phase and had a large and negative spreading coefficient. Gas competed with water to occupy the centre of the medium- and larger pores. Instead, we observed oil layers. However, these usually did not spread sandwiched between water and gas, as it happens in water-wet systems [64], but mostly adhered to the surface as thick wetting layers next to the solid surface (as in the square of Figure 6b).

Figure 8 shows a 3D representation of connected oil in a subset of the image (top row), at the end of WF1, GI and WF2. We define a wetting layer a portion of oil with thickness lower than 30 μm, as thicker volumes more likely correspond to bulky chunks of oil filling pores of small or medium size.

Oil layers were present at the end of each injection step. However, we observe fewer and thinner layers at the end of WF1, since the water pressure was high, forcing oil into smaller regions of the pore space and squeezing layers closer to the solid surface. The injection of gas allowed the formation of more layers, increasing oil connectivity (e.g. in the circle of Figure 8b).

The second row of Figure 8 shows how the thickness of these layers changed during the three injection steps. At the end of WF1, the mean thickness of connected oil layers was 13.3 ± 9.1 μm. During GI, the thickness of the layers which were already present increased, as shown by the colours in Figure 8e, while the formation of new thinner layers meant that the average thickness did not change significantly (13.0 ± 9.2 μm). During WF2, more oil was drained from these connected layers, as again water displaced oil, which decreased the layer thickness to a mean value of 10.2 ± 8.4 μm.

3.4 Gas trapping

After gas injection, the gas was not produced and its saturation remained approximately constant when water was re-injected during WF2, see Table 2. As it is mentioned in the previous section, during WF2 water mainly contacted and displaced oil, with much less direct interaction between water and gas. However, gas is indirectly affected by water injection through water-oil-gas double displacements. These double displacements have an interesting consequence: oil

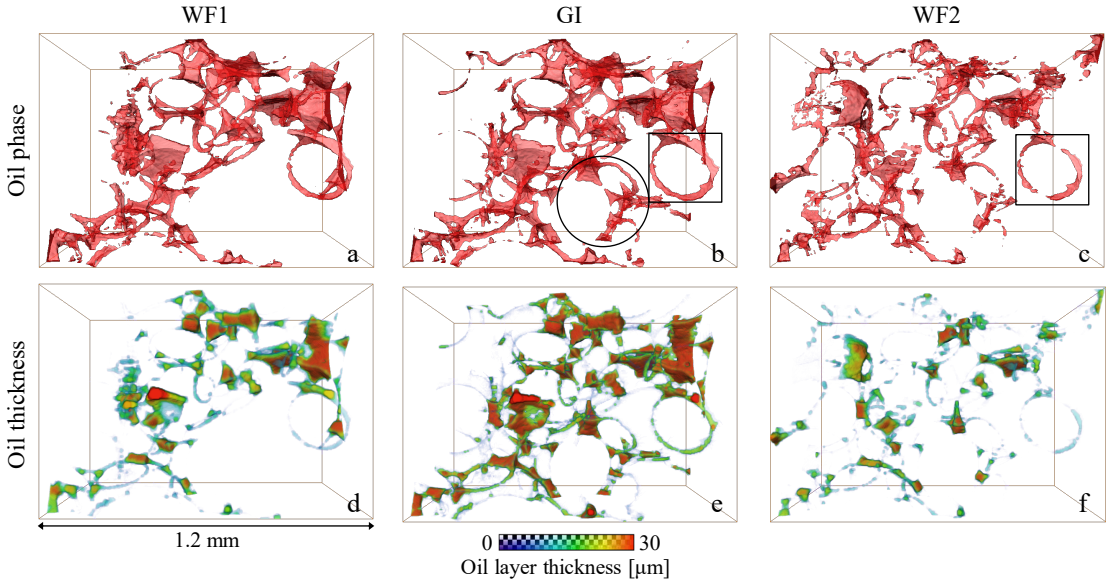

Figure 8: A-C: Three-dimensional rendering of the connected oil phase in a subset of the rock at the end of WF1, GI and WF2 respectively. In the circled region of panel B we highlighted the formation of new oil layers during GI. D-E: Thickness map of the oil phase represented in A-C.

wetting layers swell in small regions of the pore space – throats – and trap the gas by snap-off, disconnecting the gas phase in immobile ganglia that prevent gas production.

A similar gas trapping during WF2 was observed in water-wet experiments in similar rocks [64, 65]. However, there are some fundamental differences between the two cases. In water-wet media, the wettability order is water-oil-gas and at immiscible conditions oil spreads in layers, sandwiched between wetting water and non-wetting gas. The gas trapping events in these water-wet systems are double capillary trapping events, with water trapping oil which traps gas. The three-phases in fact coexist in the same pores, with the trapped ganglia of gas surrounded by spreading oil layers which are in turn surrounded by water wetting layers.

In the mixed-wet system presented in this work, instead, the wettability order is oil-water gas (Section 3.1), and the intermediate wetting phase, water, does not spread in layers, as its spreading coefficient is very negative (Section 3.3). The gas snap-off events, hence, were the consequence of single capillary trapping of the most non-wetting phase (gas) by the most wetting phase (oil), similar to what happens in two-phase flow [69, 76].

An example of these events is shown in Figure 9. We monitored a subset of the image during WF2. A fingerprint of water injection can be observed in the squared throat: water was trying to invade the small throat as its pressure increased while water was injected in the sample.

The circled throat, instead, presents an example of the double displacements mentioned above: first, at T = 15789 s, gas was pushed in the throat and in the adjacent pores through a double displacement (water-oil-gas), and later (T = 15931 s) oil snapped-off the gas occupying the circled throat and confining it as a disconnected cluster, trapped in the pore space.

This trapping mechanism within pores has consequences at larger scales: the total amount of gas trapped in this immiscible mixed-wet system was very high, with almost no production of the injected gas (Figure 10a). Previous studies have shown that, in water-wet media, gas trapping by water is higher in the presence of oil than in simple gas-water systems, as the presence of oil inhibits the direct gas-water contacts, favouring capillary trapping over piston-like displacement of gas by water. This allowed the amount of gas trapped, in three-phase systems, to increase to 60% of the gas injected, with respect to values around 50% for two-phase systems [65].

The increase of gas trapping to almost 100% of the gas injected observed in this study has to be attributed to the strikingly distinct dynamics of three-phase flow in mixed-wet media: as observed in Section 3.2, during WF2 water preferentially displaced oil, rather than directly contacting gas, as gas was surrounded by wetting and spreading layers of oil. While water displaced oil, these layers swelled in small throats like the one circled in Figure 9, trapping the

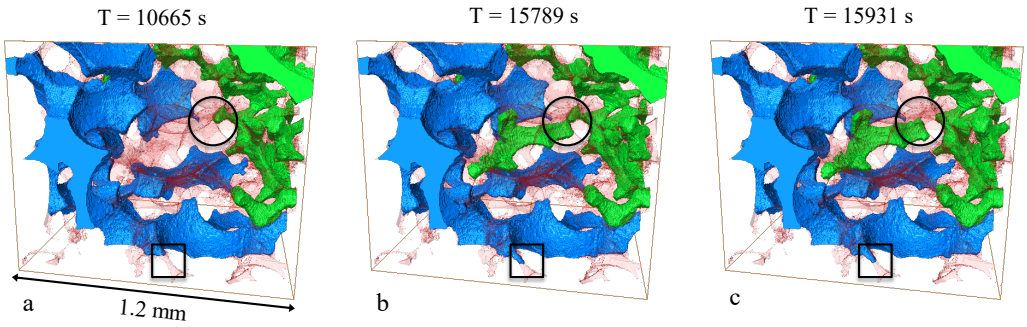

Figure 9: Three-dimensional representation of the fluids occupying the pores of a subvolume from the dynamic images during WF2. Water is blue, gas is green and oil is in semi-transparent red. In the circled throat gas invasion is highlighted (B) with subsequent gas trapping by oil (C), while the square shows a signature of WF2: water invading a small throat as its pressure increased during injection.

gas. As a result, gas trapping is favoured in immiscible mixed-wet three-phase systems, with respect to water-wet three-phase systems, which in turn presented enhanced gas trapping with respect to the two-phase case. This conclusion can have a considerable impact for gas storage applications, as discussed later.

3.5 Pore-scale descriptors (Minkowski functionals)

For a detailed elucidation of the dynamics of gas injection, we computed saturation, interfacial area, capillary pressure and Gaussian curvatures, which can be related to the Minkowski functionals, providing a complete description of the geometry of the phases in the pore space [44, 15, 65, 51].

3.5.1 Saturations

During WF1, water invaded a wide range of pore sizes, displacing and producing oil with a displacement pattern controlled by wettability [62]. After the injection of about 0.5 PV of water, the injection was stopped and the water and oil saturation were respectively 34.2% and 65.8% (Figure 10a and Table 2). Subsequent injection of gas lowered the oil saturation to 43.2%, the gas saturation increased to 23.8% while the water saturation did not change substantially, as gas mainly contacted oil (Section 3.2). Second waterflooding (WF2) caused a further decrease of oil saturation to 38.5% and an increase in water saturation to 38.6%, without a considerable change in gas saturation, due to a significant amount of gas trapping (Section 3.4).

These results suggest that immiscible gas injection, alternated with water injection, is an effective method to increase oil recovery: the total recovery factor, with respect to initial oil saturation, is 60.7%. In addition, the injected gas is retained in the pore space of the rock and was not displaced by a further injection of water: almost all the gas is not produced, as it is trapped by oil in the pore space (Section 3.4). This is promising for gas storage applications, as it suggests that chase water injection can rapidly and effectively trap the gas, ensuring secure sequestration.

3.5.2 Interfacial areas

While saturation is related to the zeroth-order Minkowski functional (the volume) the interfacial area is the first-order functional [44, 16]. The interfacial area between the phases, which was computed from the segmented images and divided by the total volume to obtain the specific interfacial area, and its evolution during the experiment, is shown in Figure 10b.

The interfacial area between oil and water increased as water was injected during WF1 and hence contacted the oil already present in the pore space. During GI, the interfacial areas again show that the injected gas mainly contacted oil (Section 3.2), causing a steep increase in the gas-oil area, while the oil-water area only slightly increased due to double gas-oil-water displacements. Throughout the displacement the gas-water area remained very low, indicating limited direct contact between gas and water: their contact was prevented by the presence of wetting and spreading oil layers (Section 3.3). During WF2, the interfacial areas did not change substantially, with the exception of an increase in the gas-oil area due to the multiple gas trapping events described in Section 3.4.

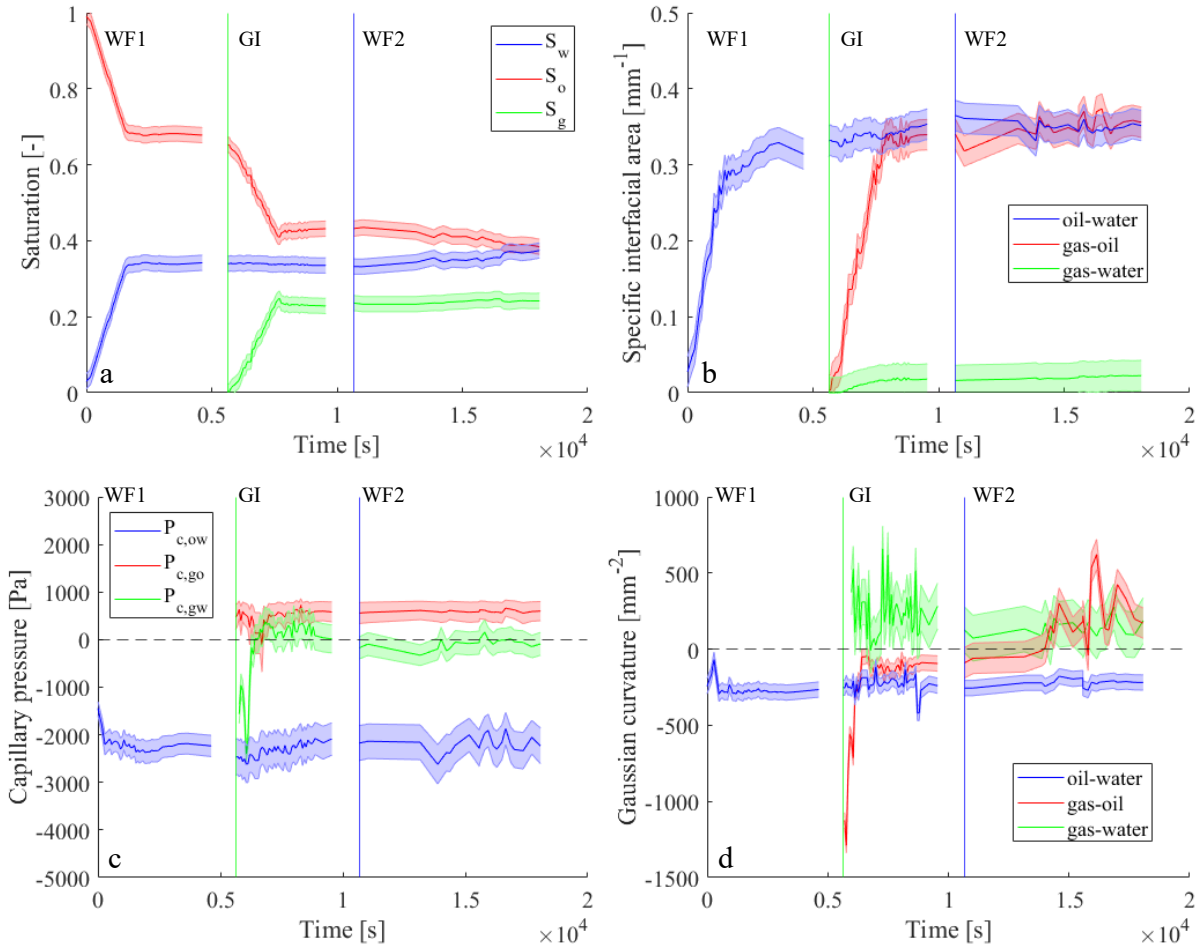

Figure 10: (A) Dynamic changes in saturations, (B) interfacial areas specific to the total volume, (C) capillary pressures and (D) Gaussian curvatures between the phases involved in the experiment. The shadowed regions indicate the standard errors of the mean values and vertical lines show when each injection started. Horizontal dashed lines were added to the capillary pressure and Gaussian curvature plots to help distinguish between positive and negative values.

3.5.3 Capillary pressure

The second-order Minkowski functional is the total curvature of the interfaces between two phases, κ_{ij}. This was computed from the segmented images following the methods developed in previous work [17, 48] and can be used to obtain the capillary pressure using the Young-Laplace equation $P_{c,ij} = \sigma_{ij}\kappa_{ij}$ (Section 2.5). Using the values of σ_{ij} reported in Table 1, we obtained the capillary pressure between the three phases during the three injection steps (Figure 10c).

The negative capillary pressure between water and oil is a consequence of the oil-wet tendency of the sample, as indicated by oil-water mean geometric contact angles higher than 90°, Figure 4 and Table 4. A negative $P_{c,ow}$ indicates that $P_w > P_o$ as water has to be forced into the oil-wet pores. The oil-water capillary pressure remains negative throughout the displacement. It does increase (become less negative) during gas injection, consistent with the slight swelling of oil layers, see Figure 8. During WF2 the capillary pressure stays approximately constant, albeit with fluctuations, even though water continues to displace oil.

The gas-oil capillary pressure remains approximately constant once gas is injected, indicating that gas needs to reach a threshold pressure to displace oil and, during WF2, to be trapped. The capillary pressure is positive, since gas is non-wetting to oil.

The gas-water capillary pressure is the most interesting, since it assumes both positive and negative values. This strengthens the observation that gas and water compete to be the most non-wetting phase. Initially, during GI the

capillary pressure is negative, as gas will preferentially invade regions of the pore space where it is wetting to water (this is an imbibition displacement). However, as evident from the saturation, the amount of direct displacement of water by gas is limited. Later, the gas-water capillary pressure becomes positive, indicating that gas reaches regions of the pore space where it is non-wetting to water. During WF2 the capillary pressure is approximately zero to within the uncertainty of the measurements, indicating no clear wettability preference. Again, however, the amount of direct displacement of gas is limited, as the gas is trapped by oil.

Unlike conventional capillary pressure measurements, our curvature-based analysis includes all interfaces, capturing both connected phases and trapped clusters. As a result, Eq. 1, which states that the gas-water capillary pressure is the sum of the oil-water and gas-oil values, is only obeyed when all three phases are connected. This is only seen at the beginning of GI: later water is trapped by gas and then, during WF2, gas is trapped by water. This change in connectivity can be quantified through the Gaussian curvature, discussed next.

3.5.4 Connectivity and Gaussian curvature

To study the potential mobility of each phase we computed their connectivity. In Figure 11, a different colour is assigned to disconnected clusters of each phase. This representation shows that oil was connected during the whole experiment. This is in contrast with previous studies of water-wet systems, where WF1 and WF2 caused the segregation of oil in many disconnected ganglia [68, 69, 64, 65]. The oil stays connected next to the pore walls as the most wetting phase, spreading in wetting layers of variable thickness (Section 3.3).

The connectivity of water was also quite high: this was connected as it was the injected phase during WF1 and WF2. Some water is trapped in pores of intermediate size during GI, but, as gas mainly displaced oil, there was not much change in the configuration of water (Section 3.2). Gas connectivity decreased during WF2, as the injection of water caused the fragmentation of gas into disconnected ganglia. This did not allow high gas recovery, and prevented its production with further water injection (Section 3.4).

Vogel *et al.* [75] showed that the third-order Minkowski functional, the Gaussian curvature of the interfaces, is directly linked to the Euler characteristic of a 3D object, which quantifies its connectivity. As a consequence, negative values of Gaussian curvature indicate a well-connected object, while positive values indicate ball-shaped objects, or trapped clusters [16, 22].

The Gaussian curvature between the phases during the experiment is shown in Figure 10d. As evident in Figure 11, both water and oil remain connected throughout the displacement and hence we see a negative Gaussian curvature between these two phases in Figure 10d. Hence, even though the sum of the curvatures, represented by the capillary pressure in Figure 10c, is negative, on average one curvature is positive while the other is larger and negative. This is a topological constraint to allow the phases to remain continuous. The Gaussian curvature between gas and water appears more noisy: as previously discussed, a small number of interfaces were formed between these two phases during the experiment (Figure 10b). At the beginning of GI it is negative, since both gas and water are well-connected. It increases and assumes a mainly positive value later as first some water is trapped, and then gas is trapped during WF2.

The gas-oil Gaussian curvature is most interesting and mirrors the connectivity of the gas phase. During GI it is negative, Figure 10d and Figure 12e, indicating that both the oil and gas phases are connected, see Figure 11. During WF2 it becomes positive, as gas is trapped and assumes, on average, a more spheroid shape.

Figure 12 shows the gas-oil curvature and quantifies how the curvatures in the principal directions κ_1 and κ_2 (where we define $\kappa_1 \geq \kappa_2$) evolved during GI and WF2. From these two curvatures, the total curvature $\kappa = \kappa_1 + \kappa_2$ and the Gaussian curvature $\kappa_g = \kappa_1 \times \kappa_2$ are calculated. At the beginning of GI (Figure 12a,e; when T=5770 s), κ_1 and κ_2 have opposite signs, leading to negative Gaussian curvature, meaning high connectivity of gas while it is injected; this connectivity was maintained until the end of gas injection (Figure 12b,f; T = 9553 s). Later, during WF2 (Figure 12c,g; T=13872 s), gas become less connected and κ_2 approached zero values indicating a flat interface in one direction, which leads to a zero Gaussian curvature. Then later all the curvatures became on average positive at the end of WF2 with a positive Gaussian curvature as the gas was trapped (Figure 12d,h; T = 18074 s).

Notice that this significant shift in the product of the curvatures occurs while the sum of the curvatures, see the dashed distributions of Figures 10a-d, was on average approximately constant, as the gas-oil capillary pressure did not change significantly (Figure 10c).

The change in κ_1 and κ_2 physically represents an evolution of the shape of the oil-gas interface. An example of a shape with curvatures with opposite signs in the two directions during GI can be observed in the squared region of Figure 8b, where the oil formed a loop while wetting a solid grain. The interface with gas at this location had a negative curvature in one direction, following the shape of the loop, and a positive value in the other direction, as gas bulges into oil. When later water was injected, the multiple displacements described in Section 3.4 caused the rupture of the gas-oil

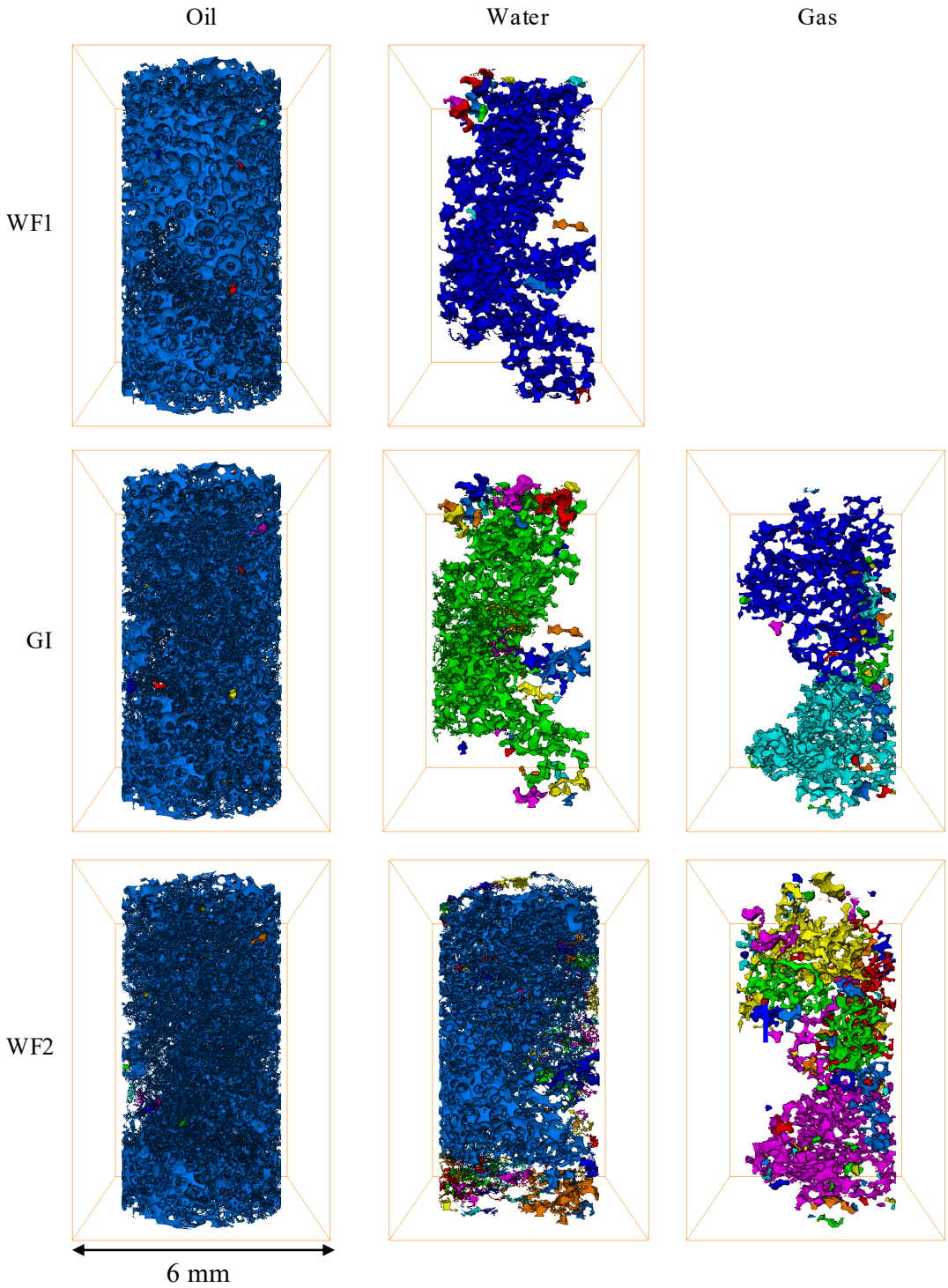

Figure 11: Connectivity of oil, water and gas at the end of the first waterflooding (WF1), gas injection (GI) and second waterflooding (WF2). Different colours represent disconnected clusters of the same phase.

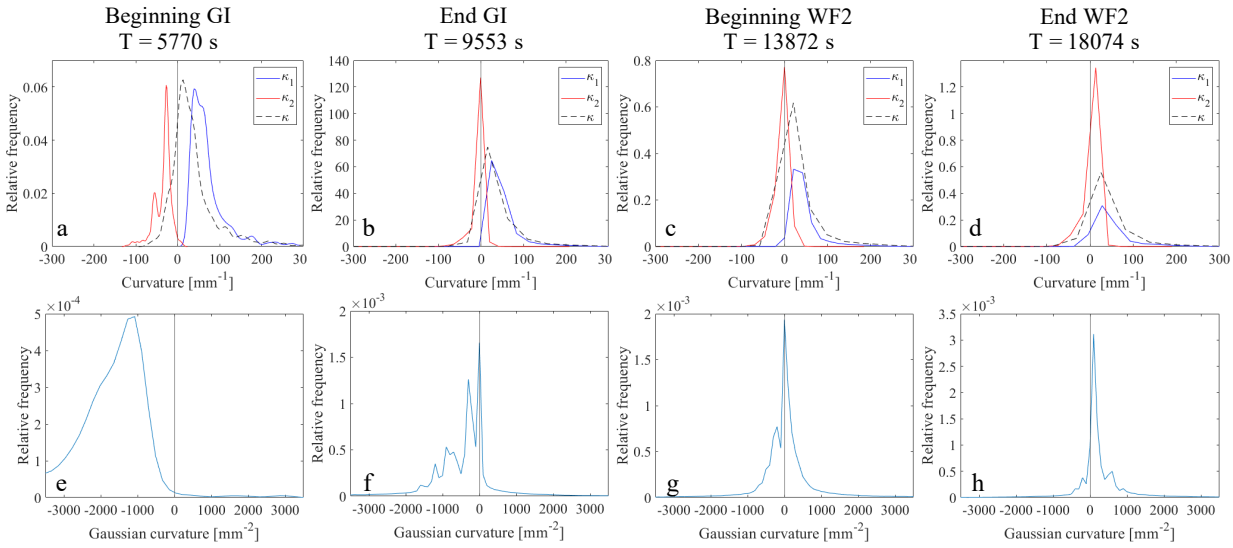

Figure 12: Focus on the gas-oil curvatures at four different times of the experiments (refer to Table 3). a-d: probability distributions of the curvatures κ_1 and κ_2 at the gas-oil interface in the two principal directions, along with the total curvature $\kappa = \kappa_1 + \kappa_2$. e-h: Gaussian curvatures $\kappa_g = \kappa_1 \times \kappa_2$.

interface, Figure 8c, changing the shape of the curvature which became on average positive in both directions (Figure 12d), resulting in gas trapping.

Overall, the capillary pressures and Gaussian curvatures provide a quantification of the key new features of three-phase flow uncovered in these experiments. In this mixed-wet system, while there are regions of the pore space that are water-wet, overall oil behaves as the most wetting phase with a negative oil-water capillary pressure and good connectivity, demonstrated by the negative Gaussian curvature of the oil-water interfaces. Gas is non-wetting to oil, and hence the gas-oil capillary pressure is positive: the Gaussian curvature of the gas-oil interface reflects the connectivity of the gas phase, being negative during GI and assuming positive values during WF2 when gas is trapped. Gas and water compete to be the most non-wetting phase with no clear wettability order: there are few direct gas-water contacts, the gas-water capillary pressure can be both less than and greater than zero, while the Gaussian curvature is positive when either water or gas are trapped.

4 Conclusions with implications for storage and recovery

We have studied the dynamics of immiscible gas injection followed by waterflooding in a mixed-wet carbonate rock sample using synchrotron X-ray imaging with high spatial and temporal resolution. We have characterized the wettability of the system measuring contact angles, pore occupancy and fluid-solid interfacial areas. As a result, the rock presented a mixed-wet behaviour with oil-water-gas wettability order, from the most to the least wetting phase. However, there is a range of wetttability across the rock, with regions that are water-wet. Furthermore, the gas is not clearly non-wetting to water and again some of the displacement occurs when gas appears to be the intermediate-wet phase.

We have shown that the displacement process is strikingly distinct from that observed in a similar water-wet system. In particular, gas directly displaced oil with negligible displacement of water, unlike in a water-wet medium, where double drainage, where gas displaces oil that displaces water, is common. During subsequent waterflooding, the principal process was direct displacement of oil by water, resulting in additional recovery. Gas was trapped by water displacing oil that then snapped-off gas in larger pores, as in a water-wet system. However, since oil was the most wetting phase, it remained continuous in wetting and spreading layers and was not trapped by water.

We quantified saturations, interfacial areas and curvatures during the displacement. From the total curvature, the capillary pressures could be estimated and used to interpret the displacement sequence that was observed. These results can also be linked to the four Minkowski functionals which provide a complete description of the geometry of the phases in the pore space, potentially facilitating theoretical developements [75, 15]. Specifically, the Gaussian curvature is a measure of connectivity and can be used to quantify the degree of trapping during the displacement. A study of the

principal curvatures of the gas-oil interface demonstrated the evolution of the fluid configurations as gas was injected and later trapped. One curvature remained positive, since gas was non-wetting to oil with a positive capillary pressure, while the other changed from being negative to zero and then positive on average as the gas became less well connected.

Our results suggest that oil recovery is favoured in this mixed-wet system, confirming previous work [57]. However, the local displacement efficiency is less favourable than observed under near-miscible conditions [4]. This corresponds to our traditional understanding of gas injection, where driving the gas and oil properties towards miscibility aids recovery [42]. More surprising though is that we see significant trapping of gas during waterflooding, which is higher than in water-wet media, which is promising for storage applications. This also implies limited gas recycling is needed during EOR schemes if gas and water are both injected.

These results can serve as benchmarks to validate and calibrate pore-scale models, and provide design criteria for engineering gas injection at the field scale. This work also has implications for the design of microfluidic devices where the wettability could be designed to produce fluid patterns and droplets with the desired structure and composition for a range of applications from food manufacture to drug delivery [28].

Future work could consider a wider range of samples, with perhaps more oil-wet conditions, and different displacement sequences. We could apply this analysis to non-geological materials, such as gas diffusion layers in fuel cells, membranes, catalysts, and microfluidic devices.

5 Acknowledgments

We acknowledge Abu Dhabi National Oil Company (ADNOC) for financial support. We are also very grateful to Amer Alhammadi and Ahmed Selem (Imperial College London) and Christoph Rau, Shashidhara Marathe, Kaz Wanelik and the staff of Diamond Light Source for their work during the experiments at the synchrotron facility.

References

[1] A. W. Adamson and A. P. Gast. *Physical chemistry of surfaces*. Wiley, 1997.

[2] A. M. Alhammadi, A. AlRatrout, K. Singh, B. Bijeljic, and M. J. Blunt. In situ characterization of mixed-wettability in a reservoir rock at subsurface conditions. *Scientific Reports*, 7(1):10753, 2017.

[3] A. M. Alhammadi, Y. Gao, T. Akai, M. J. Blunt, and B. Bijeljic. Pore-scale X-ray imaging with measurement of relative permeability, capillary pressure and oil recovery in a mixed-wet micro-porous carbonate reservoir rock. *Fuel*, 268:117018, 2020.

[4] A. Alhosani, A. Scanziani, Q. Lin, Z. Pan, B. Bijeljic, and M. J. Blunt. In Situ Pore-Scale Analysis of Oil Recovery During Three-Phase Near-Miscible CO2 Injection in a Water-Wet Carbonate Rock. *Advances in Water Resources*, page 103432, 2019.

[5] A. Alhosani, A. Scanziani, Q. Lin, A. Q. Raeini, B. Bijeljic, and M. J. Blunt. Design of safe CO2 storage in oilfields based on pore-scale fluid distribution. *In preparation*, 2020.

[6] A. H. Alizadeh and M. Piri. Three-phase flow in porous media : A review of experimental studies on relative permeability. *Reviews of Geophysics*, 52:468–521, 2014.

[7] A. AlRatrout, M. J. Blunt, and B. Bijeljic. Wettability in complex porous materials, the mixed-wet state, and its relationship to surface roughness. *Proceedings of the National Academy of Sciences of the United States of America*, 115(36):8901–8906, 2018.

[8] A. AlRatrout, A. Q. Raeini, B. Bijeljic, and M. J. Blunt. Automatic measurement of contact angle in pore-space images. *Advances in Water Resources*, 109:158–169, 2017.

[9] B. Amaechi, S. Iglauer, C. H. Pentland, B. Bijeljic, and M. J. Blunt. An Experimental Study of Three-Phase Trapping in Sand Packs. *Transport in Porous Media*, 103(3):421–436, 2014.

[10] W. Ampomah, R. S. Balch, M. Cather, R. Will, D. Gunda, Z. Dai, and M. R. Soltanian. Optimum design of CO2 storage and oil recovery under geological uncertainty. *Applied Energy*, 195:80–92, 2017.

[11] M. G. Andrew, B. Bijeljic, and M. J. Blunt. Pore-scale contact angle measurements at reservoir conditions using X-ray microtomography. *Advances in Water Resources*, 68:24–31, 2014.

[12] M. G. Andrew, H. Menke, M. J. Blunt, and B. Bijeljic. The Imaging of Dynamic Multiphase Fluid Flow Using Synchrotron-Based X-ray Microtomography at Reservoir Conditions. *Transport in Porous Media*, 110(1):1–24, 2015.

[13] I. Arganda-Carreras, V. Kaynig, C. Rueden, K. W. Eliceiri, J. Schindelin, A. Cardona, and H. S. Seung. Trainable Weka Segmentation: A machine learning tool for microscopy pixel classification. *Bioinformatics*, 33(15):2424–2426, 2017.

[14] R. T. Armstrong and S. Berg. Interfacial velocities and capillary pressure gradients during Haines jumps. *Physical Review E - Statistical, Nonlinear, and Soft Matter Physics*, 88(4):043010, 2013.

[15] R. T. Armstrong, J. E. McClure, V. Robins, Z. Liu, C. H. Arns, S. Schlüter, and S. Berg. Porous Media Characterization Using Minkowski Functionals: Theories, Applications and Future Directions. *Transport in Porous Media*, pages 1–31, 2018.

[16] R. T. Armstrong, J. E. McClure, V. Robins, Z. Liu, C. H. Arns, S. Schlüter, and S. Berg. Porous Media Characterization Using Minkowski Functionals: Theories, Applications and Future Directions. *Transport in Porous Media*, 130(1):305–335, 2019.

[17] R. T. Armstrong, M. L. Porter, and D. Wildenschild. Linking pore-scale interfacial curvature to column-scale capillary pressure. *Advances in Water Resources*, 46:55–62, 2012.

[18] F. E. Bartell and H. J. Osterhof. Determination of the Wettability of a Solid by a Liquid. *Industrial & Engineering Chemistry*, 19(11):1277–1280, 1927.

[19] R. Bellamy and O. Geden. Govern CO2 removal from the ground up. 12(11):874–876, 2019.

[20] S. Berg, H. Ott, S. A. Klapp, A. Schwing, R. Neiteler, N. Brussee, A. Makurat, L. Leu, F. Enzmann, J.-O. Schwarz, M. Kersten, S. Irvine, and M. Stampanoni. Real-time 3D imaging of Haines jumps in porous media flow. *Proceedings of the National Academy of Sciences of the United States of America*, 110(10):3755–3759, 2013.

[21] M. J. Bickle. Geological carbon storage. 2(12):815–818, 2009.

[22] M. J. Blunt. *Multiphase Flow in Permeable Media: A Pore-Scale Perspective*. Cambridge University Press, 2017.

[23] M. J. Blunt, Q. Lin, T. Akai, and B. Bijeljic. A thermodynamically consistent characterization of wettability in porous media using high-resolution imaging. *Journal of Colloid and Interface Science*, 552:59–65, 2019.

[24] K. Brown, S. Schlüter, A. Sheppard, and D. Wildenschild. On the challenges of measuring interfacial characteristics of three-phase fluid flow with x-ray microtomography. *Journal of Microscopy*, 253(3):171–182, 2014.

[25] A. Buades, B. Coll, and J. M. Morel. Nonlocal image and movie denoising. *International Journal of Computer Vision*, 76(2):123–139, 2008.

[26] T. Bultreys, W. De Boever, and V. Cnudde. Imaging and image-based fluid transport modeling at the pore scale in geological materials: A practical introduction to the current state-of-the-art. *Earth-Science Reviews*, 155:93–128, 2016.

[27] T. Bultreys, Q. Lin, Y. Gao, A. Q. Raeini, A. AlRatrout, B. Bijeljic, and M. J. Blunt. Validating model predictions of pore-scale fluid distributions during two-phase flow in rocks. *Physical Review E*, 053104(May), 2018.

[28] Z. Chen, J. Xu, and Y. Wang. Gas-liquid-liquid multiphase flow in microfluidic systems – A review. *Chemical Engineering Science*, 202:1–14, 2019.

[29] M. Feali, W. V. Pinczewski, Y. Cinar, C. H. Arns, J.-y. Arns, N. South, and M. Turner. Qualitative and Quantitative Analyses of the Three-Phase Distribution of Oil , Water , and Gas in Bentheimer Sandstone by Use of Micro-CT Imaging. *SPE Reservoir Evaluation and Engineering*, 15:706–711, 2012.

[30] D. H. Fenwick and M. J. Blunt. Three-dimensional modeling of three phase imbibition and drainage. *Advances in Water Resources*, 21(2):121–143, 1998.

[31] K. W. Ferrara, M. A. Borden, and H. Zhang. Lipid-shelled vehicles: Engineering for ultrasound molecular imaging and drug delivery. *Accounts of Chemical Research*, 42(7):881–892, jul 2009.

[32] G. Garfi, C. M. John, S. Berg, and S. Krevor. The Sensitivity of Estimates of Multiphase Fluid and Solid Properties of Porous Rocks to Image Processing. *Transport in Porous Media*, 131(3):985–1005, 2020.

[33] G. Garfi, C. M. John, Q. Lin, S. Berg, and S. Krevor. Fluid surface coverage showing the controls of rock mineralogy on the wetting state. *Geophysical Research Letters*, 47:e2019GL086380, 2020.

[34] A. Georgiadis, F. Llovell, A. Bismarck, F. J. Blas, A. Galindo, G. C. Maitland, J. P. Trusler, and G. Jackson. Interfacial tension measurements and modelling of (carbon dioxide + n-alkane) and (carbon dioxide + water) binary mixtures at elevated pressures and temperatures. *Journal of Supercritical Fluids*, 55(2):743–754, dec 2010.

[35] T. Hildebrand and P. Ruegsegger. A new method for the model-independent assessment of thickness in three-dimensional images. *Journal of Microscopy*, 185(1):67–75, 1997.

[36] G. J. Hirasaki. Structural Interactions in the Wetting and Spreading of Van Der Waals Fluids. *Journal of Adhesion Science and Technology*, 7(3):285–322, 1993.

[37] M. H. Hui and M. J. Blunt. Effects of wettability on three-phase flow in porous media. *Journal of Physical Chemistry B*, 104(16):3833–3845, 2000.

[38] A. C. Jones, C. H. Arns, A. P. Sheppard, D. W. Hutmacher, B. K. Milthorpe, and M. A. Knackstedt. Assessment of bone ingrowth into porous biomaterials using micro-CT. *Biomaterials*, 28(15):2491–2504, 2007.

[39] M. Khishvand, A. H. , and M. Piri. In-Situ Characterization of Wettability and Pore-Scale Displacements during Two- and Three-Phase Flow in natural porous media. *Advances in Water Resources*, 97(11):279–298, 2016.

[40] A. R. Kovscek, H. Wong, and C. J. Radke. A pore-level scenario for the development of mixed wettability in oil reservoirs. *AIChE Journal*, 39(6):1072–1085, 1993.

[41] A. Kundu, E. Dumont, A.-M. Duquenne, and H. Delmas. Mass Transfer Characteristics in Gas-liquid-liquid System. *The Canadian Journal of Chemical Engineering*, 81(3-4):640–646, 2008.

[42] L. Lake. *Enhanced oil recovery*.

[43] P. Laplace and J. Fournier. Sur l'action capillaire. supplément à la théorie de l'action capillaire. *Traité de mécanique céleste*, 4(Supplement 1):771–777, 1805.

[44] P. Lehmann, M. Berchtold, B. Ahrenholz, J. Tölke, A. Kaestner, M. Krafczyk, H. Flühler, and H. R. Künsch. Impact of geometrical properties on permeability and fluid phase distribution in porous media. *Advances in Water Resources*, 31(9):1188–1204, 2008.

[45] X. Li, E. Boek, G. C. Maitland, and J. P. Trusler. Interfacial tension of (Brines + CO2): (0.864 NaCl + 0.136 KCl) at temperatures between (298 and 448) K, pressures between (2 and 50) MPa, and total molalities of (1 to 5) mol·kg-1. *Journal of Chemical and Engineering Data*, 57(4):1078–1088, apr 2012.

[46] Q. Lin, B. Bijeljic, S. Berg, R. Pini, M. J. Blunt, and S. Krevor. Minimal surfaces in porous media: Pore-scale imaging of multiphase flow in an altered-wettability Bentheimer sandstone. *Physical Review E*, 99(6), 2019.

[47] Q. Lin, B. Bijeljic, S. C. Krevor, M. J. Blunt, M. Rucker, S. Berg, A. Coorn, H. Van Der Linde, A. Georgiadis, and O. B. Wilson. A new waterflood initialization protocol with wettability alteration for pore-scale multiphase flow experiments. In *Petrophysics*, volume 60, pages 264–272, 2019.

[48] Q. Lin, B. Bijeljic, R. Pini, M. J. Blunt, and S. Krevor. Imaging and Measurement of Pore-Scale Interfacial Curvature to Determine Capillary Pressure Simultaneously With Relative Permeability. *Water Resources Research*, 54(9):7046–7060, 2018.

[49] Z. Liu, A. Herring, C. Arns, S. Berg, and R. T. Armstrong. Pore-Scale Characterization of Two-Phase Flow Using Integral Geometry. *Transport in Porous Media*, 118(1):99–117, 2017.

[50] S. Marathe, M. Storm, V. S. C. Kuppilli, R. Harrison, G. Das, S. L. M. Schroeder, S. Cipiccia, F. Döring, C. David, and C. Rau. Development of synchrotron pink beam x-ray grating interferometer at the Diamond Light source I13-2 beamline. In B. Müller and G. Wang, editors, *Developments in X-Ray Tomography XII*, volume 11113, page 42. SPIE, 2019.

[51] K. R. Mecke and D. Stoyan. *Statistical Physics and Spatial Statistics*, volume 554 of *Lecture Notes in Physics*. Springer Berlin Heidelberg, Berlin, Heidelberg, 2000.

[52] N. R. Morrow. Wettability and Its Effect on Oil Recovery. *Journal of Petroleum Technology*, 42(12):1476–1484, 1990.

[53] National Institute of Standards and Technology. *NIST Chemistry WebBook*. Eds. P.J. Linstrom and W.G. Mallard, 2018.

[54] P. E. Øren, J. Billiotte, and W. V. Pinczewski. Mobilization of waterflood residual oil by gas injection for water-wet conditions. *SPE Formation Evaluation*, Volume 7:70–78, 1992.

[55] T. Pak, I. B. Butler, S. Geiger, M. I. J. van Dijke, and K. S. Sorbie. Droplet fragmentation: 3D imaging of a previously unidentified pore-scale process during multiphase flow in porous media. *Proceedings of the National Academy of Sciences of the United States of America*, 112(7):1947–52, 2015.

[56] M. Piri and M. J. Blunt. Three-dimensional mixed-wet random pore-scale network modeling of two- And three-phase flow in porous media. I. Model description. *Physical Review E - Statistical, Nonlinear, and Soft Matter Physics*, 71(2), 2005.

[57] Z. Qin, M. Arshadi, and M. Piri. Micro-scale experimental investigations of multiphase flow in oil-wet carbonates. II. Tertiary gas injection and WAG. *Fuel*, 257:116012, 2019.

[58] A. Q. Raeini, B. Bijeljic, and M. J. Blunt. Generalized network modeling of capillary-dominated two-phase flow. *Physical Review E*, 97:23308, 2018.

[59] C. Rau, M. Storm, S. Marathe, A. J. Bodey, M.-C. Zdora, S. Cipiccia, D. Batey, X. Shi, S. M. Schroeder, G. Das, M. Loveridge, R. Ziesche, and B. Connolly. Fast Multi-scale imaging using the Beamline I13L at the Diamond Light Source. In B. Müller and G. Wang, editors, *Developments in X-Ray Tomography XII*, volume 11113, page 68. SPIE, 2019.

[60] C. A. Reynolds, M. G. Andrew, H. Menke, S. Krevor, and M. J. Blunt. Dynamic fluid connectivity during steady-state multiphase flow in a sandstone. *Proceedings of the National Academy of Sciences*, 114(31):8187–8192, 2017.

[61] M. Rücker, W. B. Bartels, K. Singh, N. Brussee, A. Coorn, H. A. van der Linde, A. Bonnin, H. Ott, S. M. Hassanizadeh, M. J. Blunt, H. Mahani, A. Georgiadis, and S. Berg. The Effect of Mixed Wettability on Pore-Scale Flow Regimes Based on a Flooding Experiment in Ketton Limestone. *Geophysical Research Letters*, 46(6):3225–3234, 2019.

[62] A. Scanziani, Q. Lin, A. Alhosani, M. J. Blunt, and B. Bijeljic. Dynamics of displacement in mixed-wet porous media. *EarthArXiv*, 2020.

[63] A. Scanziani, K. Singh, M. J. Blunt, and A. Guadagnini. Automatic method for estimation of in situ effective contact angle from X-ray micro tomography images of two-phase flow in porous media. *Journal of Colloid And Interface Science*, 496:51–59, 2017.

[64] A. Scanziani, K. Singh, T. Bultreys, B. Bijeljic, and M. J. Blunt. In situ characterization of immiscible three-phase flow at the pore scale for a water-wet carbonate rock. *Advances in Water Resources*, 121:446–455, 2018.

[65] A. Scanziani, K. Singh, H. Menke, B. Bijeljic, and M. J. Blunt. Dynamics of enhanced gas trapping applied to CO2 storage in the presence of oil using synchrotron X-ray micro tomography. *Applied Energy*, 259, 2020.

[66] S. Schlüter, A. Sheppard, K. Brown, and D. Wildenschild. Image processing of multiphase images obtained via X-ray microtomography: A review. *Water Resources Research*, (50), 2014.

[67] V. Scott, R. S. Haszeldine, S. F. Tett, and A. Oschlies. Fossil fuels in a trillion tonne world. 5(5):419–423, 2015.

[68] K. Singh, B. Bijeljic, and M. J. Blunt. Imaging of oil layers, curvature and contact angle in a mixed-wet and a water-wet carbonate rock. *Water Resources Research*, 52(3):1716–1728, 2016.

[69] K. Singh, H. Menke, M. Andrew, Q. Lin, C. Rau, M. J. Blunt, and B. Bijeljic. Dynamics of snap-off and pore-filling events during two-phase fluid flow in permeable media. *Scientific Reports*, 7(1):5192, 2017.

[70] M. Sohrabi, A. Danesh, D. H. Tehrani, and M. Jamiolahmady. Microscopic mechanisms of oil recovery by near-miscible gas injection. *Transport in Porous Media*, 72(3):351–367, 2008.

[71] M. L. Szulczewski, C. W. MacMinn, H. J. Herzog, and R. Juanes. Lifetime of carbon capture and storage as a climate-change mitigation technology. *Proceedings of the National Academy of Sciences of the United States of America*, 109(14):5185–5189, 2012.

[72] M. I. J. Van Dijke and K. S. Sorbie. Pore-scale network model for three-phase flow in mixed-wet porous media. *Physical Review E*, 66:046302, 2002.

[73] M. I. J. Van Dijke and K. S. Sorbie. Three-phase capillary entry conditions in pores of noncircular cross-section. *Journal of Colloid and Interface Science*, 260:385–397, 2003.

[74] M. I. J. Van Dijke, K. S. Sorbie, M. Sohrabi, and A. Danesh. Simulation of WAG floods in an oil-wet micromodel using a 2-D pore-scale network model. *Journal of Petroleum Science and Engineering*, 52:71 – 86, 2006.

[75] H.-J. Vogel, U. Weller, and S. Schlüter. Quantification of soil structure based on Minkowski functions. *Computers & Geosciences*, 36(10):1236–1245, 2010.

[76] D. Wildenschild, R. T. Armstrong, A. L. Herring, I. M. Young, and J. W. Carey. Exploring capillary trapping efficiency as a function of interfacial tension, viscosity, and flow rate. In *Energy Procedia*, volume 4, pages 4945–4952, 2011.

[77] D. Wildenschild, J. W. Hopmans, M. L. Rivers, and A. J. R. Kent. Quantitative Analysis of Flow Processes in a Sand Using Synchrotron-Based X-ray Microtomography. *Vadose Zone Journal*, 4(1):112–126, 2005.

[78] D. Wildenschild and A. Sheppard. X-ray imaging and analysis techniques for quantifying pore-scale structure and processes in subsurface porous medium systems. *Advances in Water Resources*, 51:217–246, 2013.

[79] R. N. Zúñiga and J. M. Aguilera. Aerated food gels: fabrication and potential applications. *Trends in Food Science and Technology*, 19(4):176–187, apr 2008.